University of Kentucky

UKnowledge

Chemical and Materials Engineering Faculty Publications

Chemical and Materials Engineering

1-1-2021

The Characterization of Purified Citrate-Coated Cerium Oxide Nanoparticles Prepared via Hydrothermal Synthesis

Matthew L. Hancock
University of Kentucky, matthew.hancock@uky.edu

Robert A. Yokel
University of Kentucky, ryokel@email.uky.edu

Matthew J. Beck
University of Kentucky, m.beck@uky.edu

Julie L. Calahan
University of Kentucky, juliecalahan@uky.edu

Travis W. Jarrells
University of Kentucky, twja223@uky.edu

Follow this and additional works at: https://uknowledge.uky.edu/cme_facpub
See next page for additional authors

 Part of the Chemical Engineering Commons, and the Pharmacy and Pharmaceutical Sciences Commons

Right click to open a feedback form in a new tab to let us know how this document benefits you.

Repository Citation

Hancock, Matthew L.; Yokel, Robert A.; Beck, Matthew J.; Calahan, Julie L.; Jarrells, Travis W.; Munson, Eric J.; Olaniyan, George A.; and Grulke, Eric A., "The Characterization of Purified Citrate-Coated Cerium Oxide Nanoparticles Prepared via Hydrothermal Synthesis" (2021). *Chemical and Materials Engineering Faculty Publications*. 73.
https://uknowledge.uky.edu/cme_facpub/73

This Article is brought to you for free and open access by the Chemical and Materials Engineering at UKnowledge. It has been accepted for inclusion in Chemical and Materials Engineering Faculty Publications by an authorized administrator of UKnowledge. For more information, please contact UKnowledge@lsv.uky.edu.

The Characterization of Purified Citrate-Coated Cerium Oxide Nanoparticles Prepared via Hydrothermal Synthesis

Digital Object Identifier (DOI)
https://doi.org/10.1016/j.apsusc.2020.147681

Notes/Citation Information
Published in *Applied Surface Science*, v. 535, 147681.

© 2020 Elsevier B.V.

© 2020. This manuscript version is made available under the CC-BY-NC-ND 4.0 license
https://creativecommons.org/licenses/by-nc-nd/4.0/.

This article is freely available before October 26, 2020 at: https://authors.elsevier.com/a/1bhqUcXa%7EwHmZ

Authors
Matthew L. Hancock, Robert A. Yokel, Matthew J. Beck, Julie L. Calahan, Travis W. Jarrells, Eric J. Munson, George A. Olaniyan, and Eric A. Grulke

This article is available at UKnowledge: https://uknowledge.uky.edu/cme_facpub/73

The Characterization of Purified Citrate-Coated Cerium Oxide Nanoparticles Prepared Via Hydrothermal Synthesis

Matthew L. Hancock[a,*], Robert A. Yokel[b], Matthew J. Beck[a], Julie L. Calahan[b], Travis W. Jarrells[b], Eric J. Munson[b,#], George A. Olaniyan[a], & Eric A. Grulke[a,†]

[a]Chemical and Materials Engineering, University of Kentucky, Lexington, KY 40506-0046, United States

[b]Pharmaceutical Sciences, University of Kentucky, Lexington, KY 40536-0596, United States

*Corresponding Author, Phone: (270) 519-3963, E-mail: matthew.hancock@uky.edu

[#]Current Address: Industrial and Physical Pharmacy, Purdue University, West Lafayette, IN 47907-2091, United States

[†]Deceased November 29th, 2019

Co-Author E-mail Addresses: ryokel@uky.edu (R.A. Yokel), m.beck@uky.edu (M.J. Beck), juliecalahan@uky.edu (J.L. Calahan), twja223@uky.edu (T.W. Jarrells), munsone@purdue.edu (E.J. Munson), damilareh08@gmail.com (G.A. Olaniyan)

[Prepared for submission to Applied Surface Science]

Abstract

Hypothesis

Cerium oxide nanoparticles were synthesized using a hydrothermal approach with citric acid as a stabilizing agent. Citric acid adsorption onto the nanoceria particle surface can cease particle formation and create a stable dispersion for an extended shelf life. The product was dialyzed immediately following the synthesis to remove unreacted cerium that could contribute to biological effects. Nanoparticle characterization results are expected to help identify the surface citrate bonding structure.

Experiments

Many characterization techniques were utilized to determine size, morphology, surface properties, and citrate complexation on the nanoceria particle surface. These included transmission electron microscopy, electron energy loss spectroscopy, dynamic light scattering, x-ray diffraction, thermogravimetric analysis, Fourier-transform infrared spectroscopy, Raman spectroscopy, UV-Vis absorption spectroscopy, zeta potential, and ^{13}C solid-state nuclear magnetic resonance spectroscopy.

Findings

Primary particles were hexagonal, determined to be 4.2 nm in diameter. The hydrodynamic diameter of the dialyzed product was 10.8 nm. Each agglomerate was estimated to contain an average of 5.7 particles. The citrate coating contained 2.8 citrate molecules/nm^2, corresponding to an approximate citrate monolayer. Citrate complexation with the nanoceria surface includes the central carboxyl geminal to the hydroxyl and perhaps one of its terminal carboxyl groups.

Graphical Abstract

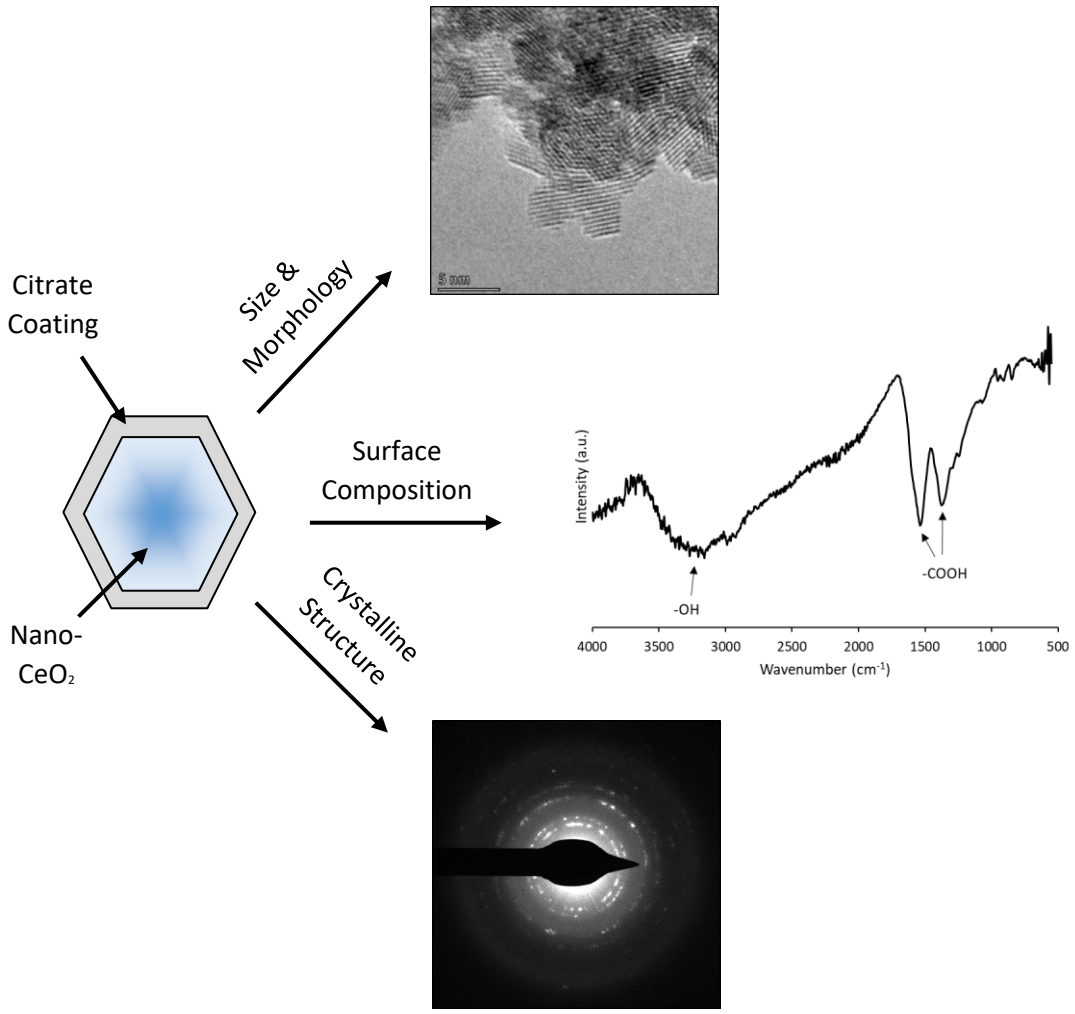

Keywords

Nanoceria; citrate-coating; hydrothermal synthesis; dialysis; characterization results; ceria-citrate complexation

Abbreviations

TEM, Transmission electron microscopy; STEM, Scanning transmission electron microscopy; EDS, Energy-dispersive X-ray spectroscopy; EELS, Electron energy loss spectroscopy; DLS, Dynamic light scattering; XRD, X-ray diffraction; SAED, Selected area electron diffraction; TGA, Thermogravimetric analysis; FTIR, Fourier-transform infrared spectroscopy; ^{13}C-SSNMR, Carbon-13 solid-state nuclear magnetic resonance spectroscopy

Highlights

- Cerium ions, known to produce adverse biological effects, are removed by dialysis
- Characterization of citrate-coated nanoceria prepared via hydrothermal synthesis
- Results include size and morphology, surface composition, and crystallinity
- Investigation of the ceria-citrate complexation bonding structures

1. Introduction

1.1 Background

Ceria (CeO_2) has been utilized in oxidative catalysts [1, 2], engine exhaust purification [3], diesel fuel additives [4], UV absorbing materials [5, 6], sunscreens [7, 8], heat resistant alloy coatings [9], solid oxide fuel cells [10], solid electrolytes [11], semiconductor manufacturing [12], and polishing [13]. There is high interest in nanosized materials due to their unique material properties, low manufacturing cost, decreased toxicity, and greater mobility than the bulk material. Nanoceria particles are useful in a variety of material, chemical, and medical applications. Interest has recently sparked for nanoceria use in biomedical applications [14, 15]. The therapeutic potential of nanoceria includes treating/addressing cancer [16, 17], radiation-induced damage [18, 19], cardiac dysfunction [20, 21], neurodegenerative diseases [22, 23], retinal degeneration [24, 25], and wounds [26] to name a few.

For nanoceria particles to be effective in biomedical applications, small size with little variance, and high colloidal stability are instrumental for positive, meaningful outcomes. The oxidative stress effects of larger (≥ 30 nm) ceria particles and its biodistribution from blood revealed cerium concentrated in the spleen and liver, but little in the brain [27, 28]. The toxicity of nanoceria is quite low, however large aggregated ceria particles produced granuloma in the lungs and liver, and fibrosis in the lungs [28-30]. Aggregated nanoparticles are generally immunotoxic, while stable, non-aggregated nanoparticles show little to no toxicity [31]. Dissolution studies have shown nanoceria degradation in acidic environments, accelerated by carboxylic acids, as present in phagolysosomes and in the plant rhizosphere. The dissolution rate was determined to be directly proportional to the particle surface area [32, 33]. Exposure of citrate-coated nanoceria particles to simulated lung, gastric, and intestinal fluids resulted in loss or overcoating of the surface citrate, and in some cases, agglomeration [34]. Ceria is a well-known redox catalyst, which provides the basis as a versatile material to be used in a wide variety of applications. The cerium atoms on the surface can store or release oxygen, cycling between Ce^{3+} and Ce^{4+} ions [35-37]. A reduction of particle size is typically accompanied by an increase in Ce^{3+} ions. An increase of Ce^{3+} ions and oxygen vacancies within the crystal structure causes lattice strain which increases the lattice parameter [38].

Nanoceria can be stabilized and particle growth (agglomeration) prevented by coating with citric acid [39-41]. The negative charges present on citric acid's carboxylic acid groups act as repelling agents with other citrate-coated nanoceria particles to create a stable, colloidal sol. Analysis of 3-10 nm nanoceria particles revealed that they were predominantly truncated octahedrals [42]. The understanding of nanoparticle behavior in the environment is important due to concerns for their potential to interact with drinking water systems and reservoirs. The uncertainties come from the lack of understanding of their surface structure and energies [43].

Numerous methods have been used and reported to fabricate nanoceria particles including precipitation [44, 45], sol-gel [46, 47], spray hydrolysis [48], spray pyrolysis [49], sonochemical [50, 51], microemulsion [52], microwave-assisted hydrothermal [53, 54], and hydrothermal [39, 55, 56]. This work is based on a hydrothermal method, which produces ~5 nm nanoceria relevant to environmental and biological applications. The objective was to prepare a pure product, to avoid cerium ion contamination, and characterize, in detail, citrate-coated nanoceria to further understand the properties of a nanoparticle coating interface. Many characterization techniques were implemented to determine size, morphology, surface properties, and citrate complexation on the surface of nanoceria particles.

1.2 Cerium Ion Toxicity

To obtain a pure nanoceria product, it is necessary to remove the unreacted cerium ion. Ceria nanoparticles and the cerium ion interact differently within biological systems. The cerium ion is more active and toxic compared to ceria nanoparticles. Stark [57] clearly distinguished molecules, or ions, and nanoparticles as completely separate entities that operate via differing mechanisms in biological milieu. He also notes that the failure to yield reliable experimental results is a direct result of the lack of understanding of the differences between particles and molecules. Therefore, unreacted cerium should be removed from nanoceria following its synthesis.

Compared to the cerium ion, nanoceria particles are less toxic. The cerium ion might contribute to biological effects that should not be attributed to nanoceria. In previous studies, a 100 mg cerium ion/kg intravenous (IV) injection was lethal to rats, while only three of eight rats died following an IV injection of 250 mg of 5 nm nanoceria/kg [58]. Pulmonary inflammatory responses to 0.1 mg/kg cerium ion were observed, however there were no such changes from 1 mg/kg nanoceria [59]. The LD_{50} of cerium chloride in mice was approximately 13 mg/kg [60]. In addition, IV injection into dogs of 50 mg/kg cerium chloride resulted in deterioration over 21 days [61]. When 9 and 18 mg/kg cerium ion was injected into rats, they experienced severe hepatotoxicity, including fatty liver and jaundice [62]. In contrast, doses up to 100 mg/kg of 5, 15, 30, and 50 mg/kg of 55 nm ceria in rats were tolerated for 30 days [63]. Once the cerium ion enters into the blood steam, it can cause aggregation of plasma proteins [64]. Toxic effects of high dose rare earth elements (REE), such as cerium, are related to enzyme activity. REEs can enter cells and bind with macromolecules, and therefore inhibit bodily functions [65].

The pharmacokinetics of nanoceria and cerium ion are also quite different. Four hours following IV injection of 5, 15, or 30 nm nanoceria or cerium ion into rats, nanoceria was removed from the blood faster than the free ion [58]. Molina et al. [59] compared the lung clearance of intratracheal (IT) instilled 40 nm nanoceria to cerium ions. Both materials showed slow clearance. After 28 days, 88% of nanoceria and 74% of cerium ion remained in the lungs. However, in extrapulmonary organs, only 0.9% of nanoceria and 6.0% of the cerium ion dose were retained. On the other hand, fecal and urinary cerium ion elimination was much higher than nanoceria. Significant amounts of cerium ion were retained in most tissues 28 days post-installation, with most in the bone and liver. This relates well to Yokel et al. [28] where 72% of the total nanoceria dose found in organs was present in the liver, spleen, and bone marrow after 90 days. Furthermore, 15 days after an IV injection of cerium chloride, 20, 16, 2, and 2% was in the skeleton, liver, kidneys, and gastrointestinal (GI) tract, whereas 0.7, 0.5, 0.08, 0.08, and 0.05% was in the muscle, spleen, lung, testes, and heart, respectively [66, 67].

The potential toxicity is low for inhaled, ingested, or injected nanoceria, however the same is not true for free cerium ions. Longer tissue retention times, coupled with higher free cerium ion toxicity, supports the need to remove free cerium before injection of nanoceria. Furthermore, the pharmacokinetics of each are not analogous. The separation of cerium ions from nanoceria solutions is critical in order to obtain reliable experimental results.

1.3 Cerium Citrate Complexation

How citrate is bound to the cerium ion has been reported as a variety of possible coordination complexes [68]. Leal [69] suggested the formula $(Cit)_2Ce^{3-}$, however the actual structure, i.e. the exact location of Ce-O bonds, is unknown. Ohyoshi et al. [70] studied, by ion exchange, complexes resembling $M(H_2Cit)^+$, $M(H_2Cit)_2^-$, MHCit, and $M(HCit)_2^{3-}$, where 'M' represents lanthanides. Again, the structures were not determined, but insight into the number and location of bonds between cerium and deprotonated carboxylic acids would help to understand the complex formation. Further studies of citrate complexation with lanthanides led to the suggestion of bifurcated and/or chelated bonds between carboxylic acid oxygen groups and the metal ion [71-75]. Baggio and Perec [76] reported a polymeric lanthanum citrate complex consisting of bridged O-C-O groups with a repeat unit of $[La(HCit)(H_2O)]$. This suggests the possibility of multiple citrate molecules bound to one Ce ion and the idea of a multilayer coating surrounding a metal oxide core. Getsova et al. [77] indicated HCitH as a common bonding molecule to cerium containing one protonated carboxylic group, and reported that one Ce^{3+} ion can be bonded to ligands participating in other cerium citrate complexes. Zhang et al. [40] proposed possible structures of cerium citrate complexation and suggested the possibility of up to three citrate molecules bound to one cerium cation. Chen et al. [78] reported formation of dimeric complexes of lanthanide trihydrates with citrate or malate. Models of MHCit and $MCit^-$ are shown in Fig. 5 of Heller et al [79] where 'M' refers to Cm or Eu. The confirmed complexations of MHCit and $MCit^-$ are determined based on the location of IR spectrum peaks. Grulke et al. [32] computed the formation energy of single and bi-ligand citrate-nanoceria complexes in comparison to nanoceria, which revealed in order of stability: bi-ligand complexes > nanoceria > single-ligand complexes. Bidentate chelating configurations were also reported as being favored over bridging and monodentate configurations. Auffan et al. [80] used ATR-FTIR and ^{13}C-NMR to show that citrate formed a chelate with Ce(IV) on the nanoceria surface through its central carboxyl and its α-hydroxyl groups. Much is still unknown about the complexation of citrate on the nanoceria surface. However, surface ceria citrate complexation will help address these research gaps.

2. Experimental

2.1 Materials

The following chemicals, including their sources, purity, and CAS #s, used in the nanoceria synthesis, and adjustment of osmolarity and pH were: cerium(III) chloride heptahydrate, Sigma, 99.9%, 18618-55-8; citric acid monohydrate, Fisher, ACS grade, 5949-29-1; ammonium hydroxide, Sigma, ACS grade (28% NH_3 in H_2O), 1336-21-6; sodium nitrate, VWR, ACS grade, 7631-99-4; sodium hydroxide, VWR, ACS grade, 1310-73-2; and nitric acid, Sigma, ACS grade, 7697-37-2. Lacey carbon, 300 mesh, copper grids (product #01895) from Ted Pella, Inc. were used for electron microscopy. Dialysis tubing from Ward's Science (product #s 470163-404 & 470163-408) with a MWCO of 12-14 kDa was used for dialysis against citric acid and DI water. The citric acid-1,5-$^{13}C_2$ used to produce nanoceria to be analyzed by ^{13}C-NMR was from Sigma, 98%, 302912-06-7.

2.2 Synthesis & Purification Methods

Nanoceria was synthesized using a hydrothermal method based on Masui et al. [39]. A cerium chloride heptahydrate and citric acid monohydrate mixture was added to ammonium hydroxide and stirred. The final concentrations were 0.25 M cerium chloride, 0.25 M citric acid, and 1.5 M ammonium hydroxide. The mixture was transferred to an autoclave for 24 h at 50 °C, and then another 24 h at 80 °C. The product was then dialyzed against 0.11 M (iso-osmotic) pH 7.4 citric acid for 120 h, replacing the dialysate every 24 h, to remove excess cerium salts (Ce ions) and ammonium hydroxide. This was then dialyzed against DI water for an additional 72 h, replacing the dialysate every 24 h, to remove unbounded citric acid from the solution. The dialysate volume was 10x the nanoceria dispersion volume. The resulting mixture was a stable, well-dispersed sol of ceria nanoparticles dispersed in DI water. It was stored under refrigeration protected from light. For the instruments that required dry powder, the dispersion was lyophilized for 48 h.

2.3 Characterization Techniques

Transmission Electron Microscopy (TEM)

The nanoceria sol was diluted with DI water to 0.5 mg/mL, and sonicated for 10 minutes in a sonication bath. A lacey carbon, 300 mesh, copper grid was dipped into the solution for approximately 5 seconds and dried overnight at room temperature. Electron microscopy was performed on a Thermo Scientific Talos F200X. The instrument was operated at an accelerating voltage of 200 keV. TEM images were recorded on a Ceta CCD camera, and particle size distributions were determined using ImageJ software. The mean size (μ) and its standard deviation (σ) were computed and the low and high range of measured diameters were reported. Energy-dispersive X-ray spectroscopy (EDS) and electron energy loss spectroscopy (EELS) were completed on the sample using Thermo Scientific's SuperX G2 and Gatan's Enfinium ER, respectively.

Dynamic Light Scattering (DLS)

Dispersions (0.5 mg/mL) were prepared in water and sonicated for 10 minutes. Using the Brookhaven 90Plus Particle Size Analyzer, five analysis runs of five minutes each were completed for the pre-dialysis, post-citrate, and post-water dialysis samples, and the average result of each run was analyzed and recorded. All samples were evaluated using the multimodal setting.

X-ray Diffraction (XRD)

Double-sided sticky tape was attached to a glass microscope slide and dried powder was distributed across the tape. Measurements were made using a Siemens D500 X-ray diffractometer with Cu Kα radiation. The analysis was conducted from 25 to 60 degrees 2θ, 0.01 degree step size, and a speed of 1 degree/min. Sharp, distinct peaks in the XRD spectra indicate a crystalline structure.

Thermogravimetric Analysis (TGA)

TGA (PerkinElmer TGA7) was used to determine the organic weight percent of the sample, in this case, the weight percent of citric acid bound to the nanoceria surface. This was repeated five times to get an accurate result of the overall weight percent of citrate. All runs were completed under a nitrogen atmosphere to prevent organic matter oxidation, resulting in pyrolysis of any organic matter on the nanoparticle surface. The sample was heated from 20 to 125 °C at 10 °C/min, held at 125 °C for 30 minutes to release physisorbed water, and then heated to 900 °C at 10 °C/min. The weight loss of the sample beyond 125 °C was taken to be the weight percent of citrate present on the surface. The amount of citrate groups was computed using the results from TGA and the particle size analysis from TEM images.

Fourier Transform Infrared Spectroscopy (FTIR)

A Nicolet 6700 FTIR with a diamond ATR crystal was used to detect organic functional groups on the nanoparticle surface. Lyophilized nanoceria was placed on the crystal and 32 scans were completed, which was then duplicated using a 2nd batch of coated nanoceria. Peaks at 1365 and 1535 cm^{-1} wavelengths are attributed to the carboxylic acid functional groups present in citric acid.

Raman Spectroscopy

Nanoceria particles were placed on a glass microscope slide. The Raman spectra of the samples were analyzed on a Thermo Fisher Scientific DXR Raman microscope equipped with an Olympus brand microscope and a 10x working distance objective. A 780 nm Raman laser with the power set to 10.0 mW was used for sample analysis. The spot size of the laser beam was 3.1 μm. All Raman spectra were collected in a spectral range of 2500–50 cm^{-1}. Each Raman spectrum was an average of five accumulations consisting of 5 seconds each.

Zeta Potential

An Anton Paar Litesizer 500 Particle Analyzer was used to determine the zeta potential of nanoceria dispersions at 0.5 mg/mL. 100 runs were completed in sequence with a 30 second equilibration time at 25 °C. The instrument was equipped with a 40 mW laser emitting at a wavelength of 658 nm. Zeta potential was determined once at each point between pH 0.5 and 13. Nitric acid and sodium hydroxide were used to adjust the pH.

UV-Vis Spectroscopy

A BioTek Synergy 2 Plate Reader was used to perform UV spectroscopy. The spectra were collected from 270 to 410 nm wavelength at a step rate of 5 nm. Each spectrum was an average of three total replications at each concentration.

Carbon-13 Solid-state Nuclear Magnetic Resonance Spectroscopy (^{13}C-SSNMR)

CP/MAS NMR data was collected using a home-built Tecmag Redstone NMR Spectrometer (Houston, TX), Bruker 300 MHz magnet (Billerica, MA), and Chemagnetics (Ft. Collins, CO) NMR probe with 7.5 mm rotors spinning at 4000 Hz. A relaxation delay of 2 seconds was used with 256 acquisition points and 20,480 scans and 1 ms CP contact time. TNMR software (Houston, TX) was used to process the data. 3-methylglutamic acid was used as a reference standard, with the methyl peak referenced to 18.84 ppm.

3. Results & Discussion

3.1 Particle Size & Morphology

The size and morphology of the synthesized, purified, nanoceria were initially characterized by TEM. Fifty particles in Figure 1a were measured via ImageJ. The average diameter was 4.24 nm, standard deviation 1.18 nm, and range 2.07 to 6.38 nm. The particles appear to be hexagonal as shown in Figure 1b.

EDS mapping using dark field STEM was also completed on the nanoceria product as shown in Figure 2. Cerium and oxygen were found as expected. It is interesting to note that the nanoceria was only found on the edges of the lacey carbon film and protruded into vacuum spaces on the copper grids. This is evident in Figures 1 and 2 as well as other TEM and STEM images obtained in this study, see Figures 2-4, 2-5, and 2-6 of Hancock [81].

EELS can provide information about the relative contribution of Ce^{3+} or Ce^{4+} to nanoceria's surface oxidation state. The ionization edges in the high-loss region of the EELS spectrum are affected by the oxidation state of the elements present in the sample. Charge transfer between atoms due to oxidation reduces the screening effect on the ejected electron. The binding energy increases, shifting the ionization edges farther right on the EELS spectrum. The relative intensities of the M5 and M4 peaks are directly related to Ce^{3+} and Ce^{4+} concentrations, respectively, as shown in Turner et al. [82]. Figure 3 shows the M5/M4 peak heights for the nanoceria (a) core and (b) surface. The M5 peak is equivalent in height to M4 in the particle core, representing primarily Ce^{4+}. However, on the surface, the M5 peak is greater than M4, representing primarily Ce^{3+}.

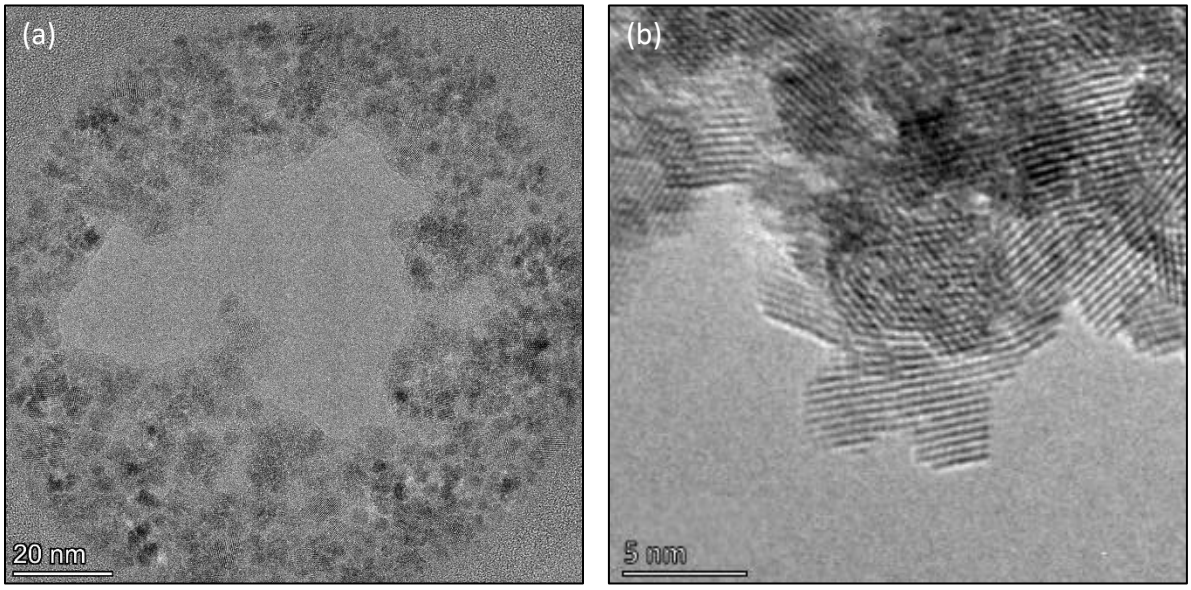

Figure 1: TEM images of nanoceria: (a) Low magnification TEM image of nanoceria agglomerate where agglomeration appears to be due to drying on the copper grid. (b) High magnification TEM image of individual crystalline nanoceria hexagonal particles.

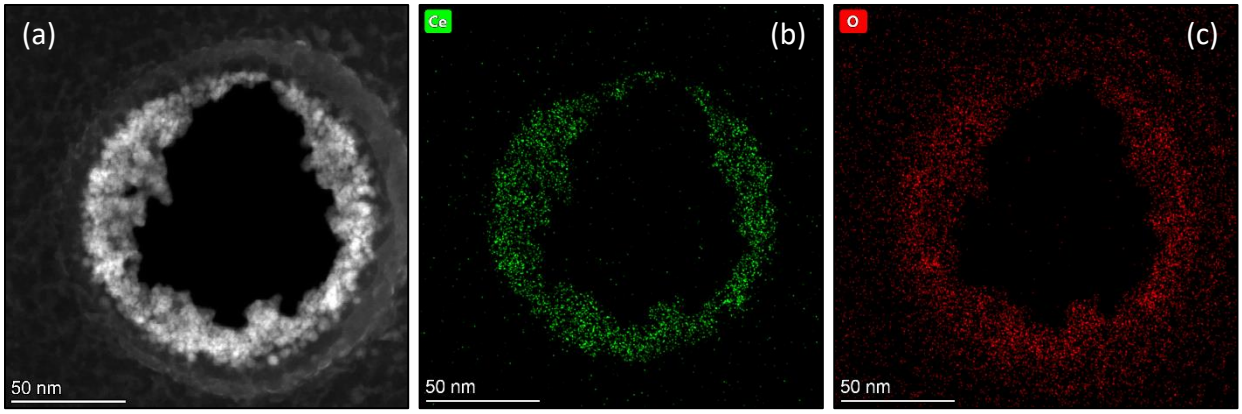

Figure 2: STEM/EDS of nanoceria: (a) Dark field STEM image of nanoceria particles, (b) EDS map of cerium, (c) EDS map of oxygen.

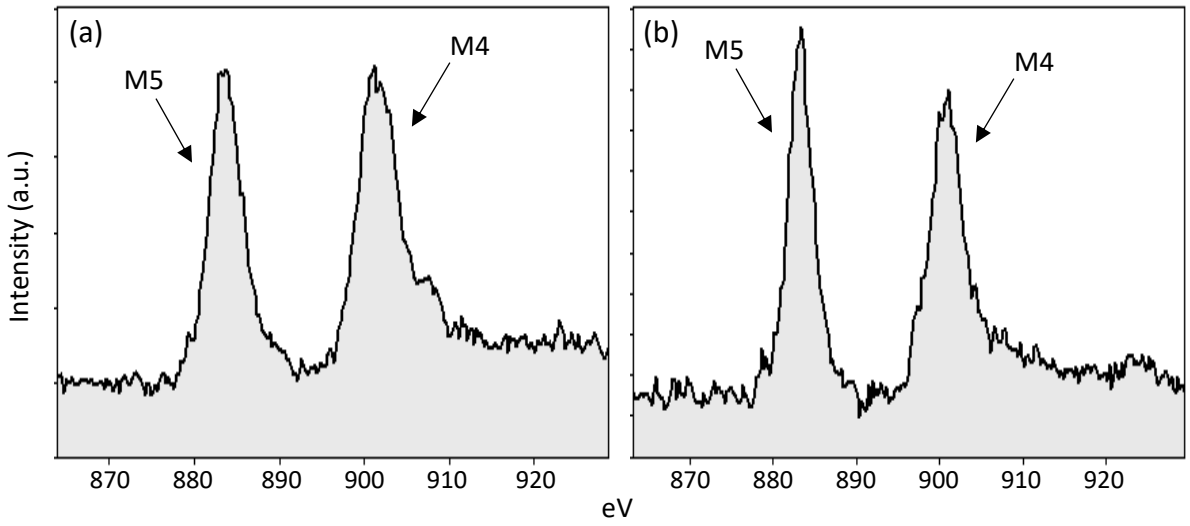

Figure 3: EELS analysis of nanoceria particles with labeled M5 and M4 peaks: (a) The M5 peak is equivalent in height to M4 in the particle core; (b) The M5 peak is greater than M4 on the particle edge.

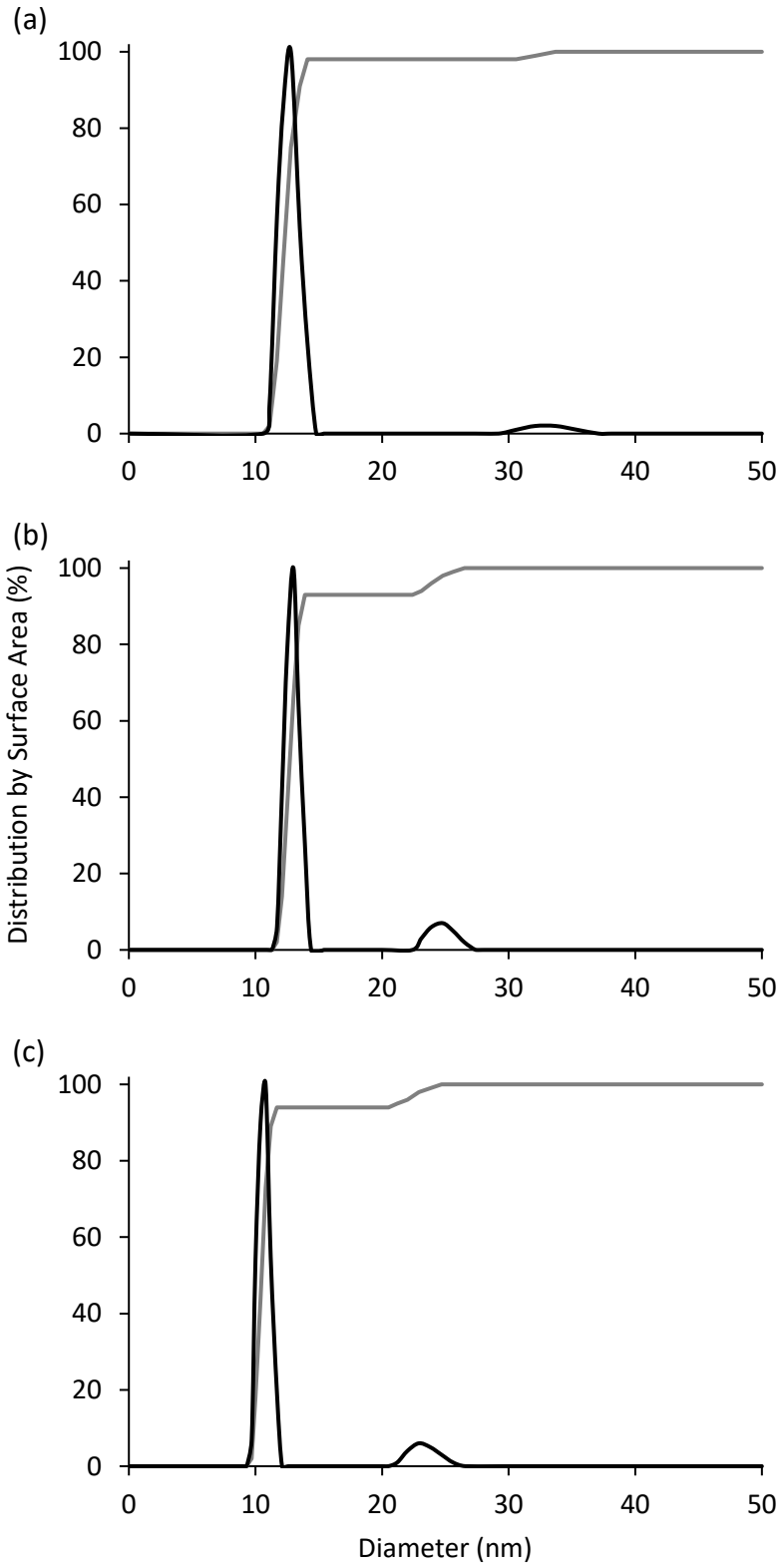

Figure 4: DLS of nanoceria – Black: Distribution, Gray: Cumulative: (a) pre-dialysis, (b) post-citrate dialysis, & (c) post-water dialysis.

DLS was completed at all stages of the synthesis: pre-dialysis, post-citrate dialysis, and post-water dialysis (Figure 4). All three samples had bimodal distributions. The 1st peak contains more than 90% of the sample by surface area percent. There is a small decrease in size, from approximately 12.8 to 10.8 nm hydrodynamic diameter (1st peak) after both sets of dialysis.

The hydrodynamic diameter is not equivalent to the primary particle diameter as determined by TEM. Thus, it appears that in solution the particles are slightly agglomerated. This is common among a variety of metal oxide nanomaterials. It is possible to estimate the number of particles per agglomerate. The fractal dimension is a variable used to define agglomerate morphology, which can vary depending on particle density within an agglomerate. The fractal dimension is expressed as follows (Equation 1):

$$N_p = A\left(D_g / D_p\right)^{D_f} \quad (1)$$

Where N_p is the number of primary particles in the agglomerate, A is a dimensionless prefactor, D_g is the characteristic diameter of the agglomerate, D_p is the primary particle diameter (determined by TEM to be 4.24 nm), and D_f is the fractal dimension [83]. The number of particles was counted in predetermined circles with known diameters. Circular areas were drawn onto the TEM image with diameters of 10, 15, 20, 25, and 30 nm, and individual particles were counted inside each area. These results were linearized and graphed, and a best-fit line fit to the data as shown in Figure 5. The slope is equal to the fractal dimension, D_f (1.64), and the intercept can be used to determine the prefactor, A (1.23). Table 1 shows the number of particles (N_p) in each circular area with diameter, D_g. Using Equation 1, the number of particles present in a 10.8 nm agglomerate is estimated to average 5.7.

Table 1: The number of particles (N_p) in each circular area with diameter, D_g.

D_g (nm)	N_p	$\log(D_g/D_p)$	$\log(N_p)$
10	5	0.377	0.699
15	10	0.553	1.00
20	16	0.678	1.20
25	23	0.775	1.36
30	30	0.854	1.48
D_f	1.64		
A	1.23		

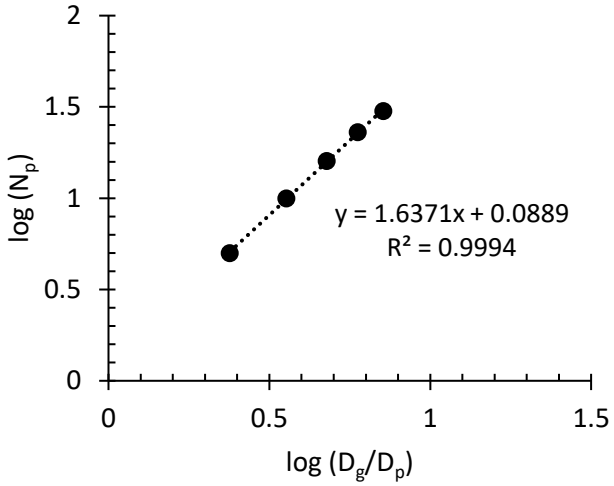

Figure 5: Fractal analysis of the nanoceria agglomerates.

3.2 Crystalline Structure

Nanoceria's XRD pattern matches that of face-centered cubic fluorite, cited as JCPDS card no. 34-0394 [84-86] and ICDD card no. 04-013-4361 [87, 88]. The diffraction peaks are labeled as shown in Figure 6 and matched to the selected area electron diffraction (SAED) pattern (Figure 7) obtained from TEM. The peaks are broad, representing that of a small crystallite size. The average particle size (D) was estimated using the Scherrer equation, where k is a constant (0.9), λ is the wavelength of the x-ray (0.154 nm), β is FWHM (full width at half maximum), and θ is the diffraction angle as shown in Equation 2:

$$D = \frac{k\lambda}{\beta cos\theta} \tag{2}$$

The average particle diameter is 5.15 nm, as shown in Table 2. This is within standard error of the size analysis of the TEM images. The small difference could be due to instrumental broadening. The interplanar spacing, d_{hkl}, for each crystal plane with Miller indices (*hkl*) was calculated using Bragg's law as shown in Equation 3. The lattice parameter (crystal lattice side length), a, was then calculated as follows (Equation 4) and was found to be 5.41 Å, further confirming face-centered cubic fluorite crystal structure:

$$2d_{hkl}sin\theta = \lambda \tag{3}$$

$$\frac{1}{{d_{hkl}}^2} = \frac{1}{a^2}(h^2 + k^2 + l^2) \tag{4}$$

Table 2: XRD data for the nanoceria particles.

Miller Indices (*hkl*)	**XRD Peaks (2θ)**	**FWHM (°)**	**Diameter (nm)**	**d_{hkl} (Å)**	**Lattice Parameter (Å)**
(111)	28.6	1.6	5.12	3.12	5.40
(200)	33.1	1.4	5.92	2.70	5.40
(220)	47.5	1.8	4.82	1.91	5.41
(311)	56.3	1.9	4.74	1.63	5.41
		Avg. Diameter	5.15 nm		

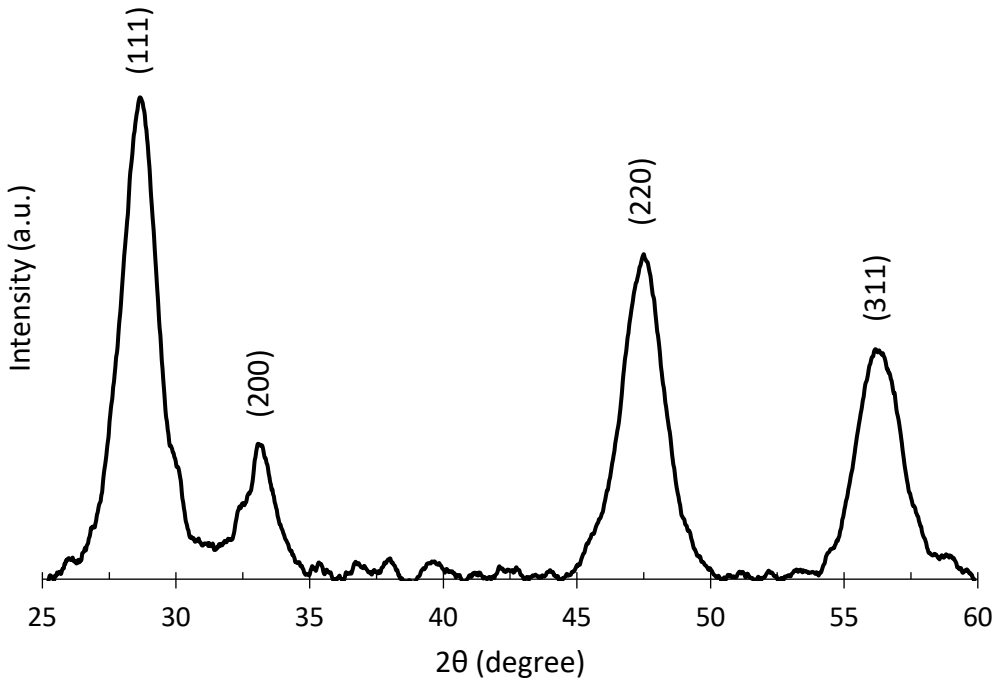

Figure 6: The XRD pattern for the nanoceria particles including crystal planes.

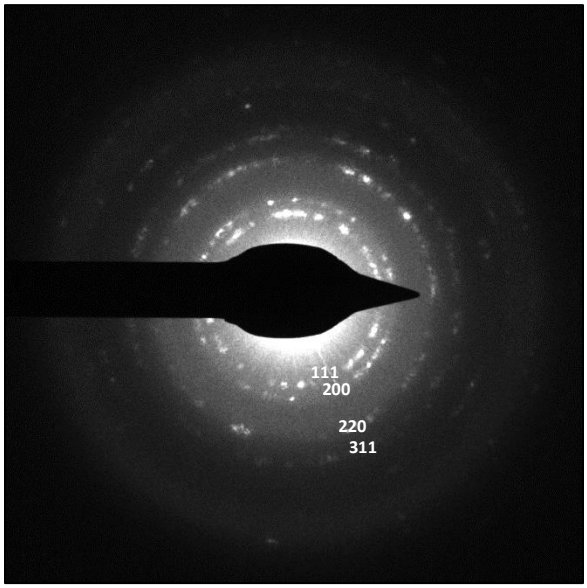

Figure 7: SAED pattern of the nanoceria particles including crystal planes.

3.3 Surface Composition

The nanoceria surface is coated with citric acid. The citrate molecules are adsorbed to the ceria particle surface and serve two purposes. First, they prevent further growth of the core ceria particle by restricting cerium ion access. Second, they prevent aggregation by repelling neighboring particles due to their net negative charge. The result is a stable colloidal sol of citrate-coated nanoceria particles less than 15 nm in diameter.

TGA was completed on the lyophilized particles to determine the percentage of free water and citrate present on the surface. Approximately 5% by weight is composed of free water present on the surface, determined by holding the temperature at 125 °C for 30 minutes. The TGA curve from 125 to 900 °C is shown in Figure 8. The weight dropped by 15% that can be attributed to citric acid. The weight percent of citric acid can be used to determine the number of citrate molecules per nm^2 on the particle surface (Equation 5), similar to Larsen et al. [89]:

$$A = \frac{W\rho r N_A}{3M_W(1-W)} \quad (5)$$

Where A is the number of citrate molecules/nm^2, W is the percent weight loss, ρ is the density of the core particle (7.22 g/cm^3), r is the particle radius, N_A is Avogadro's number, and M_W is the molecular weight of citric acid (192.1 Da). Assuming a core diameter of 4.24 nm (as determined by analyzing the TEM images), there are approximately 2.82 citrate molecules per nm^2, corresponding to 160 citrate molecules on the surface of each CeO_2 particle. This would result is a coating thickness of approximately 4.44 Å. The average diameter of citric acid molecules is in the range from 0.57 (hydrodynamic) to 0.72 nm (crystal state) [90]. This would mean that the surface is between 70 and 115% covered [91]. Therefore, on average, a citrate monolayer is present on the nanoceria surface.

In addition, the number of cerium ions on the surface of each particle can be estimated by calculating the number of CeO_2 unit cells present within one particle, using the lattice parameter as determined by XRD, 5.41 Å. Assuming a core diameter of 4.24 nm, there are approximately 1,000 CeO_2 molecules per particle, 390 of which are on the surface. See Figure 9 for the graph of the number of surface cerium ions in relation to the particle diameter. Therefore, there are 160 citrate molecules bound to 390 cerium atoms. This indicates that two cerium atoms are potentially bound to one citrate molecule.

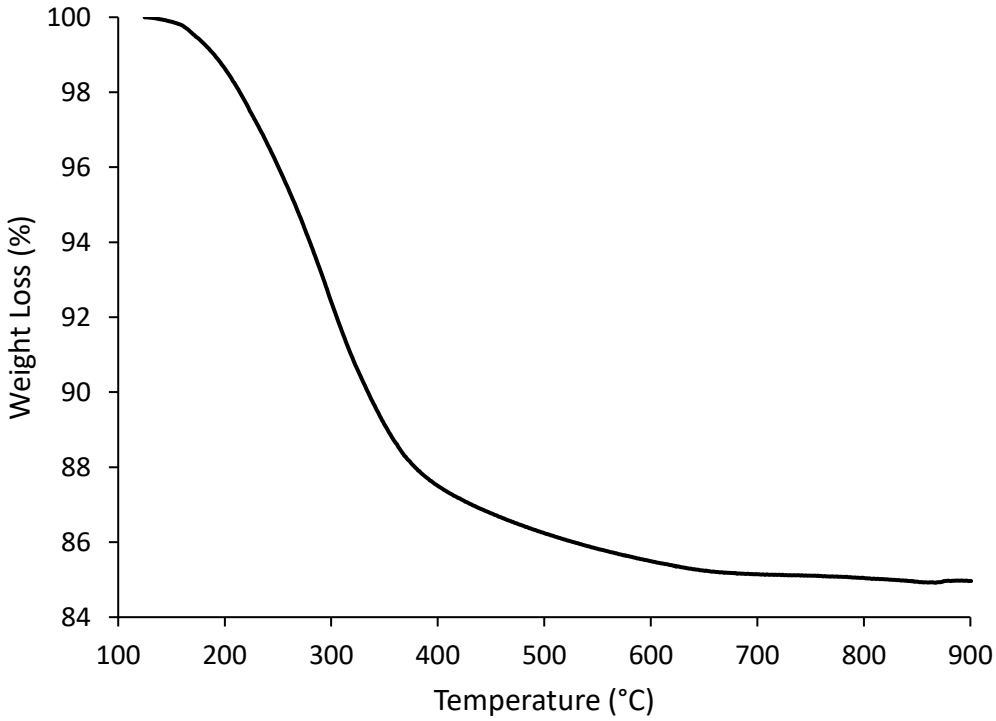

Figure 8: TGA weight loss of nanoceria attributed to citric acid.

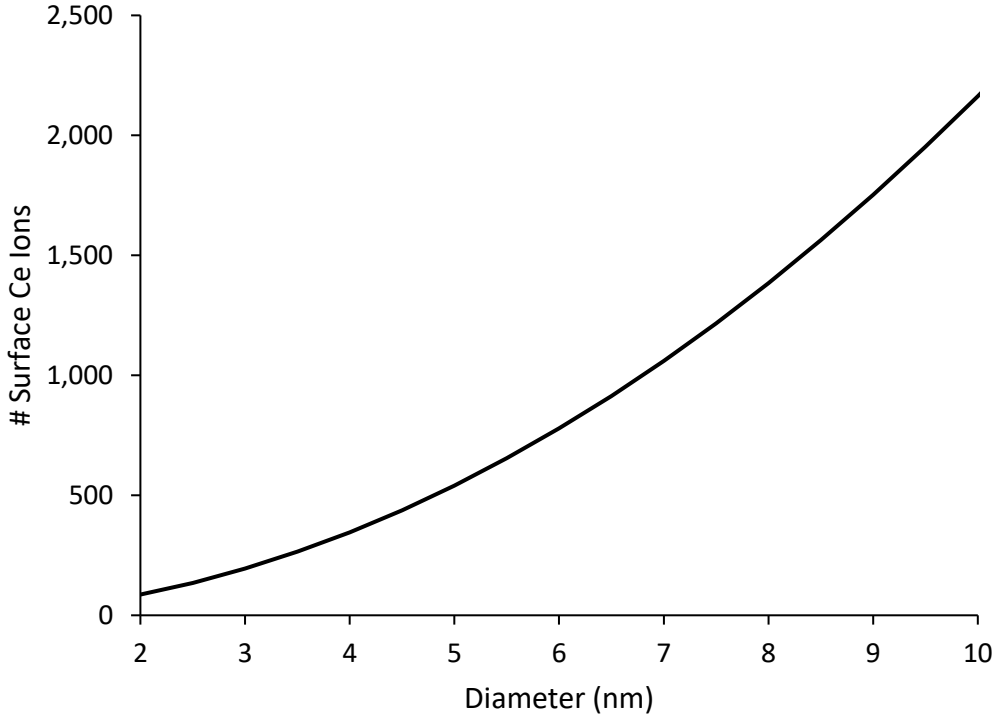

Figure 9: The number of surface cerium ions in relation to the particle diameter.

Figure 10 shows the FTIR spectrum of the citrate-coated nanoceria. The broad peak around 3200 cm^{-1} resembles the stretching band of a hydroxyl group. The peaks at 1535 and 1365 cm^{-1} are attributed to the antisymmetric and symmetric stretching band of a carboxyl group, respectively, confirming citric acid bonding to the nanoceria surface.

The peaks are similar to the peak locations of the dual strong peaks present in Fig. 3: Heller et al. [79] – 1568 and 1390 cm^{-1} vs. 1535 and 1365 cm^{-1}. Keep in mind that the metals used in that study were Cm and Eu. This could mean that the ligand is any of the $HCitH_2^-$, $HCitH^{2-}$, $HCit^{3-}$, or Cit^{4-} species, depending on the pH. The IR spectra trend shows that the peak location wavenumber decreases as the ligand becomes more deprotonated, i.e. the pH increases. The pH of the pre-dialysis solution is 9.81, which decreases to 8.52 post-citrate dialysis, and then to 7.67 post-water dialysis. The neutral pH post-dialysis with citric acid and water is expected. According to Heller et al. [79], citrate molecules between a pH of 6 and 12 are $HCit^{3-}$. This species presents a wide variety of possible citrate complexes on the nanoceria surface given the deprotonation of three of the four possible hydroxides (three carboxyls and one hydroxyl).

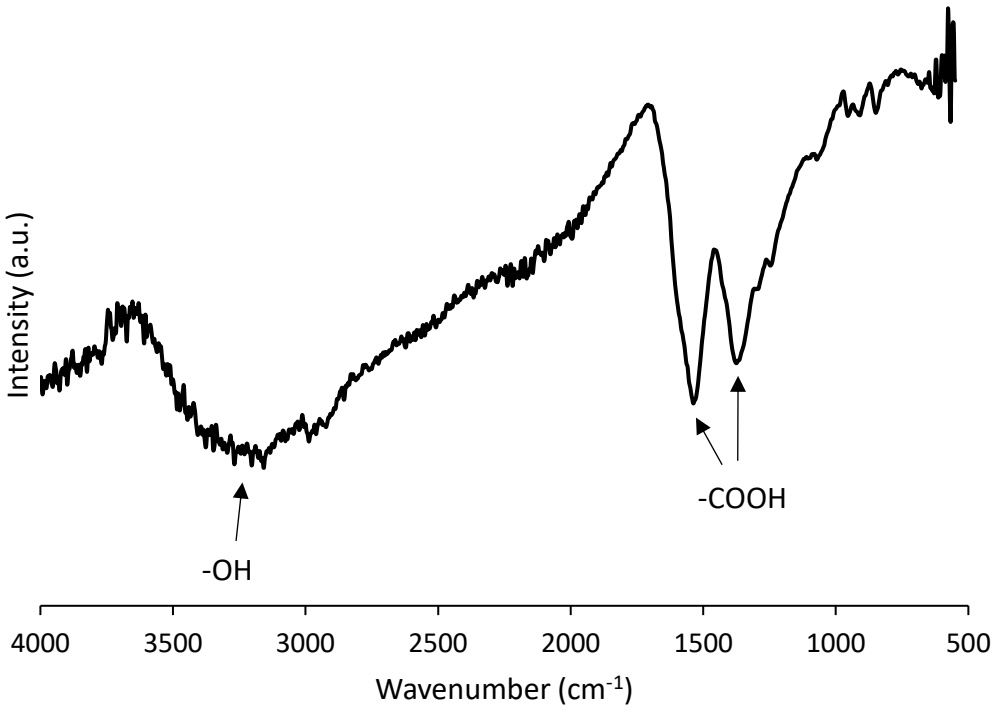

Figure 10: FTIR spectrum of citrate-coated nanoceria.

Figure 11 shows the citrate-coated nanoceria Raman spectrum. The peak at 465 cm^{-1}, which contains F_{2g} symmetry typical among fluorite structure metal dioxides, is described as a symmetric breathing mode of oxygen atoms surrounding the cerium ions [92]. The small peaks at 940 and 780 cm^{-1} are representative of citric acid on the surface of the nanoceria. Unlike the FTIR peaks, the citric acid peaks are barely noticeable. The peak around 1400 cm^{-1} is due to the microscope slide holding the sample. Similar to the XRD peaks, the broad peaks are attributed to the small particle size. In addition, other factors such as lattice strain, and consequently, valence, may affect the Raman peak size and shift [53].

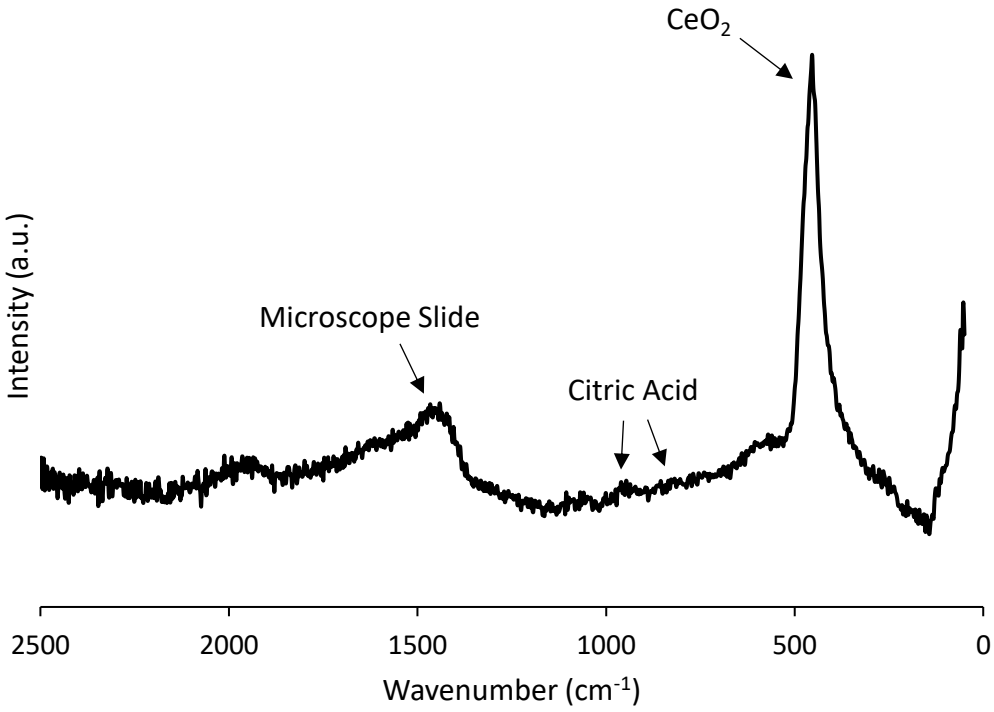

Figure 11: Raman spectrum of citrate-coated nanoceria.

The zeta potential was determined for the citrate-coated nanoceria sol from pH 0.5 to 13 as shown in Figure 12. The zeta potential determines the charge of a particle in suspension. A zeta potential greater than +30 or less than -30 mV decreases the potential for agglomeration in the medium due to repulsive electrostatic forces [93]. The data was fitted using the Carreau model, which has been previously used to model zeta potential, ζ, as a function of pH [91], as shown in Equation 6:

$$\frac{\zeta - \zeta_\infty}{\zeta_0 - \zeta_\infty} = [1 + (a \cdot 10^{pH})^2]^{(b-1)/2} \quad (6)$$

Where ζ_∞ is the limiting zeta potential at high pH, ζ_0 is the limiting zeta potential at low pH, and a and b are constant coefficients. The model predicted the isoelectic point (IEP) at pH 1.41. Agglomeration occurred below pH 2 and above pH 12. A plateau was not observed at a low pH, however the high pH plateau was estimated up to a pH of 12. The ζ_∞ was estimated to be -42.7 mV. The citrate coating prevents agglomeration and contains negative charges that lower the zeta potential values. The model fit the data quite well up to pH 3.5. Above pH 3.5 and through the circumneutral range, the zeta-potential is representative of good colloidal stability.

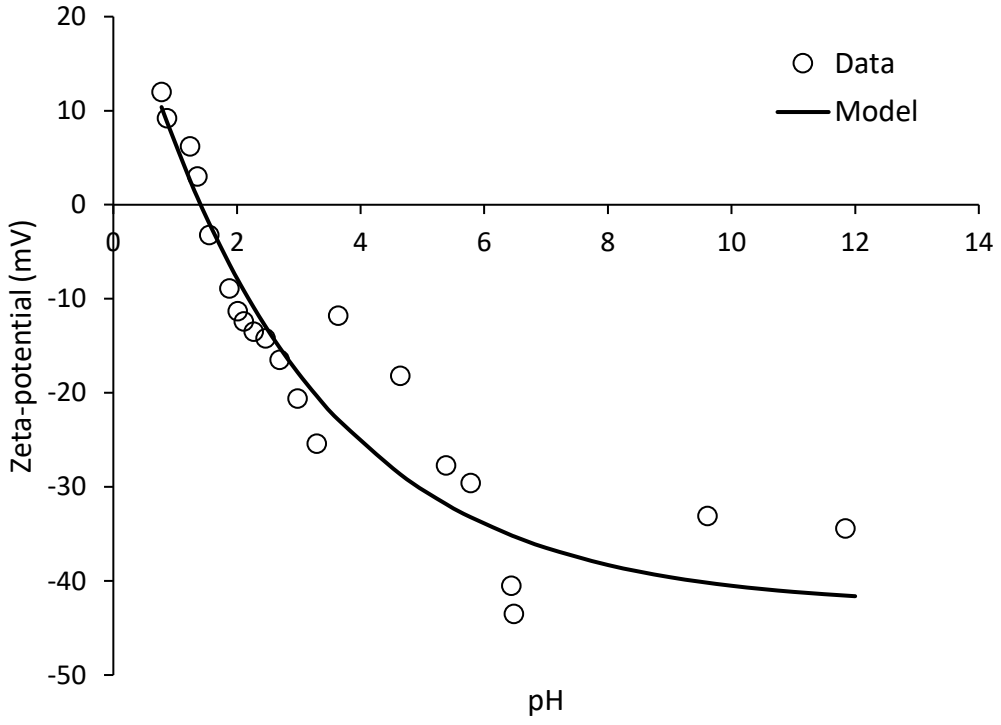

Figure 12: Zeta potential of citrate-coated nanoceria with fitted Carreau model.

Figure 13 shows the UV-Vis spectra of citrate-coated nanoceria. Ceria absorbs light from a wavelength of 270 to 370 nm, well within the UV region. Five concentrations are shown; some of the readings were too high for the instrument to read, therefore the graphs were terminated at that point. They were included to show greater UV absorption at higher wavelengths for the larger nanoceria concentrations, but the absorption is still in the same region as the lower concentrations. A decrease in nanoparticle size has been reported to shift the UV adsorption edge to lower wavelengths [56].

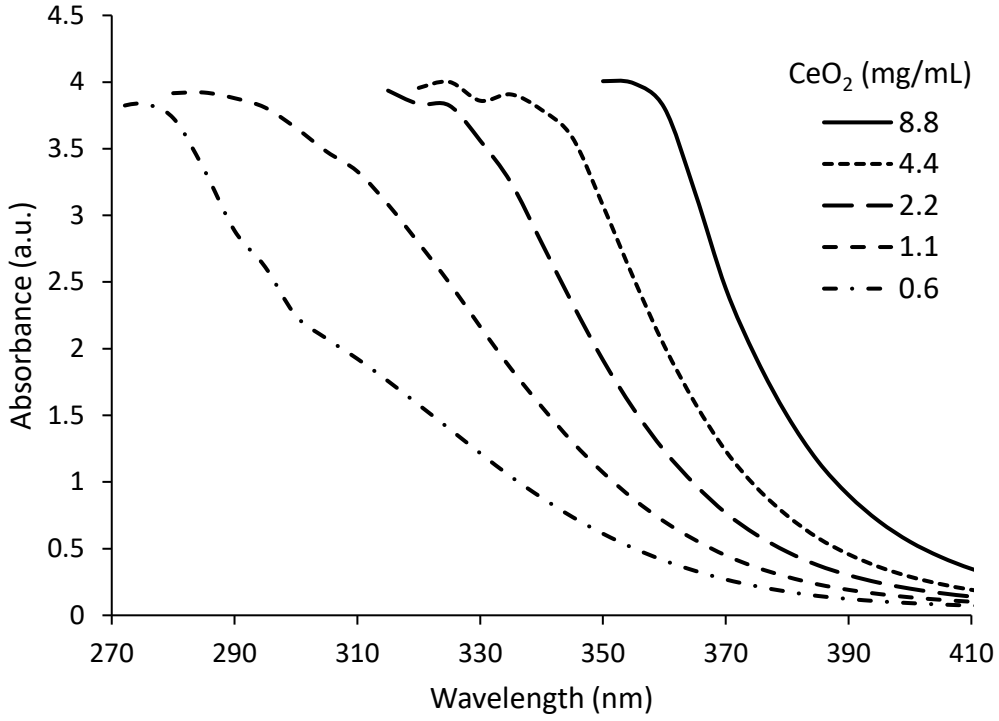

Figure 13: UV-Vis spectra of citrate-coated nanoceria.

^{13}C-SSNMR was conducted on the lyophilized particles coated with unlabeled and ^{13}C-labeled citric acid. The labeled citric acid was only partially labeled. The terminal -COOH groups (C2) contained ^{13}C. The results are shown in Figure 14 and compared to the citric acid reference. The labeled spectrum indicates that citrate bonded to the nanoceria particle during synthesis and was retained through dialysis due to the C2 peak of the labeled nanoceria. In addition, the peak shifts at 87 and 165 ppm (dashed lines) may be a result of the C3 and either C2 or C1 carbons bonding to the nanoceria surface, respectively. This would suggest that the central carbon bonded to the hydroxyl (C3) group and either the central carboxyl (C1), one of the terminal carboxyls (C2), or perhaps two of the three total carboxyls participate in complexation with the nanoceria surface. The original C3 peak at 78 ppm remains which means that either free citric acid is still present or there is a possible combination of citrate bonding mechanisms. These results are similar to Auffan et al. [80]; they suggest that citrate formed a chelate with cerium through its central carboxyl and its α-hydroxyl groups.

Possible ceria-citrate complexes are shown in Figure 15. According to the TGA analysis results, it is likely that two cerium atoms are bound to one citrate molecule, which indicates that at least two oxygen atoms are complexing with ceria, thus rejecting model 1. ^{13}C-NMR results indicate that the central carbon bonded to the hydroxyl (C3) appears to be interacting with ceria. This would reject models 1 and 3, at least as favored complexes. According to the FTIR peak locations and pH measurements, the citrate $HCit^{3-}$ species favors model 5 if all three of the deprotonated oxygens participate in bonding with ceria. However, ^{13}C-NMR shows a large portion of the end carbon atoms bonded to the carboxylic acids (C2) remain unbonded to cerium, which could consist of any combination of the five models shown or more. One possibility that arises from the ^{13}C-NMR results, and supported by Auffan et al. [80], is that the carboxylic acid functional group (C1) geminal to the central hydroxyl (C3) is favored to complex with ceria. This is shown in model 2 and again in model 5, accompanied by a terminal carboxyl (C2) bond.

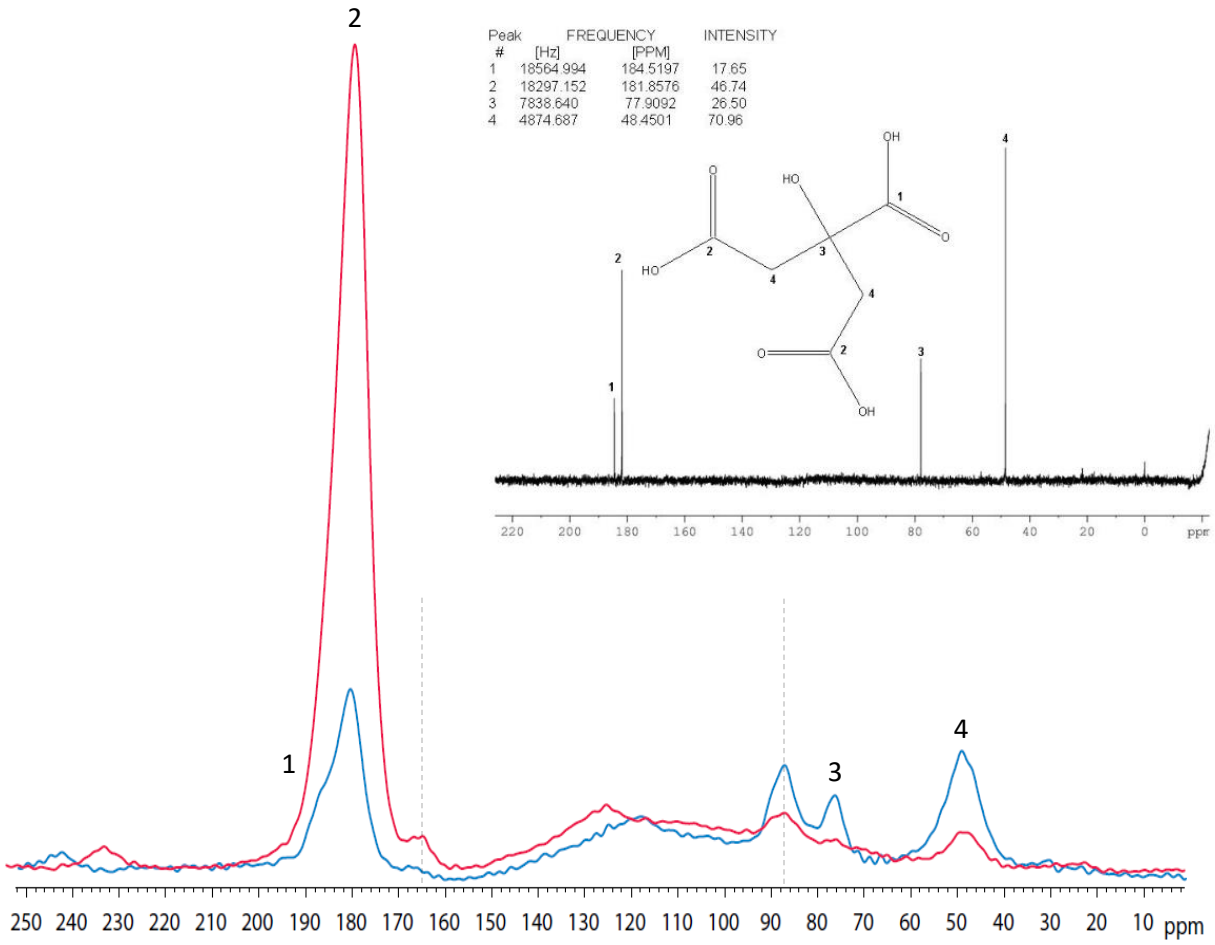

Figure 14: ^{13}C-NMR spectra of ^{13}C-labeled (red) and unlabeled (blue) citric acid. Inset is the citric acid reference (DrugBank ID# DB04272) with numbered carbon atoms. Dashed lines are placed at 87 and 165 ppm.

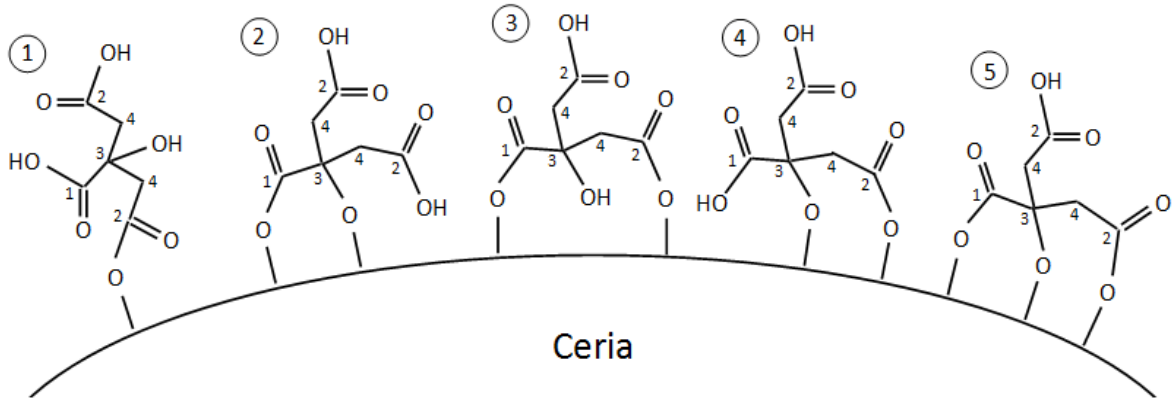

Figure 15: Suggested bonding structures modeling ceria-citrate complexation representing analysis of TGA, FTIR, and ^{13}C-NMR results.

4. Conclusions

Citrate-coated nanoceria particles were produced via hydrothermal synthesis and dialyzed against citric acid and water to remove unreacted cerium ions and salts. Characterization techniques were implemented to determine particle size and morphology, crystalline structure, and surface composition and properties. TEM revealed the particles to be hexagonal and 4.24 nm in diameter with a standard deviation of 1.18 nm. EELS indicated that the core is primarily Ce^{4+}, while the surface contains primarily Ce^{3+} atoms. The XRD and SAED pattern matches the face-centered cubic fluorite crystal structure. The crystallite diameter was calculated to be 5.15 nm using XRD peaks, similar to TEM image analysis results. A 15% weight loss due to citric acid was determined by TGA and FTIR, which corresponds to 2.82 citrate molecules/nm^2 nanoceria surface. The zeta potential was largely negative at a neutral pH with an IEP at pH 1.41. ^{13}C-NMR supports that the central carboxyl geminal to the hydroxyl complexes with ceria. In addition, one of the terminal carboxyls may also bond with ceria. This extensive physicochemical characterization of a purified nanoceria that has a size amenable to material, chemical, and medical applications will help in the selection for use and interpretation of results from such studies.

Author Contributions

M.L. Hancock: Conceptualization, Validation, Formal Analysis, Investigation, Writing – Original Draft, Visualization; **R.A. Yokel**: Writing – Review & Editing, Supervision, Funding Acquisition; **M.J. Beck**: Writing – Review & Editing, Supervision; **J.L. Calahan**: Formal Analysis, Investigation; **T.W. Jarrells**: Formal Analysis, Investigation; **E.J. Munson**: Formal Analysis, Supervision; **G.A. Olaniyan**: Formal Analysis, Investigation; **E.A. Grulke**: Writing – Review & Editing, Supervision, Project Administration, Funding Acquisition

Acknowledgements

This work is funded by the National Institutes of Health under Award Number R01GM109195. The content is solely the responsibility of the authors and does not necessarily represent the official views of the National Institutes of Health. E.J. Munson is a partial owner of Kansas Analytical Services, a company that provides solid-state NMR services to the pharmaceutical industry. The results presented here are from academic work at the University of Kentucky and no data from Kansas Analytical Services is presented here. The authors acknowledge support from Dali Qian (TEM), Nancy Miller (XRD), Freddy Arce (Raman), Andrew Colburn (Zeta potential), and Landon Mott (UV-Vis). The authors would also like to thank Marsha Ensor for her contribution.

References

1. Kim, H.J., et al., *Design of ceria catalysts for low-temperature CO oxidation.* ChemCatChem, 2020. **12**(1): p. 11-26.
2. Lykaki, M., et al., *Impact of the synthesis parameters on the solid state properties and the CO oxidation performance of ceria nanoparticles.* RSC Advances, 2017. **7**(10): p. 6160-6169.
3. Bekyarova, E., et al., *CO oxidation on Pd/CeO_2–ZrO_2 catalysts.* Catalysis Today, 1998. **45**(1-4): p. 179-183.
4. Dale, J.G., et al., *Transformation of cerium oxide nanoparticles from a diesel fuel additive during combustion in a diesel engine.* Environmental Science & Technology, 2017. **51**(4): p. 1973-1980.
5. Tsunekawa, S., et al., *Origin of the blue shift in ultraviolet absorption spectra of nanocrystalline CeO_{2-x} particles.* Materials Transactions, JIM, 2000. **41**(8): p. 1104-1107.
6. Yamashita, M., et al., *Synthesis and microstructure of calcia doped ceria as UV filters.* Journal of Materials Science, 2002. **37**(4): p. 683-687.
7. Masui, T., et al., *Synthesis of BN-coated CeO_2 fine powder as a new UV blocking material.* Journal of Materials Chemistry, 2000. **10**(2): p. 353-357.
8. Yabe, S. and T. Sato, *Cerium oxide for sunscreen cosmetics.* Journal of Solid State Chemistry, 2003. **171**(1-2): p. 7-11.
9. Patil, S., et al., *Synthesis of nanocrystalline ceria particles for high temperature oxidation resistant coating.* Journal of Nanoparticle Research, 2002. **4**(5): p. 433-438.
10. Yahiro, H., et al., *High temperature fuel cell with ceria-yttria solid electrolyte.* Journal of the Electrochemical Society, 1988. **135**(8): p. 2077-2080.
11. Inaba, H. and H. Tagawa, *Ceria-based solid electrolytes.* Solid State Ionics, 1996. **83**(1-2): p. 1-16.
12. Speed, D., et al., *Physical, chemical, and in vitro toxicological characterization of nanoparticles in chemical mechanical planarization suspensions used in the semiconductor industry: towards environmental health and safety assessments.* Environmental Science: Nano, 2015. **2**(3): p. 227-244.
13. Hedrick, J.B. and S.P. Sinha, *Cerium-based polishing compounds: discovery to manufacture.* Journal of Alloys and Compounds, 1994. **207**: p. 377-382.
14. Walkey, C., et al., *Catalytic properties and biomedical applications of cerium oxide nanoparticles.* Environmental Science: Nano, 2015. **2**(1): p. 33-53.
15. Thakur, N., P. Manna, and J. Das, *Synthesis and biomedical applications of nanoceria, a redox active nanoparticle.* Journal of Nanobiotechnology, 2019. **17**(1): p. 84.
16. Gao, Y., et al., *Cerium oxide nanoparticles in cancer.* OncoTargets and Therapy, 2014. **7**: p. 835.
17. Pešić, M., et al., *Anti-cancer effects of cerium oxide nanoparticles and its intracellular redox activity.* Chemico-Biological Interactions, 2015. **232**: p. 85-93.
18. Madero-Visbal, R.A., et al., *Harnessing nanoparticles to improve toxicity after head and neck radiation.* Nanomedicine: Nanotechnology, Biology and Medicine, 2012. **8**(7): p. 1223-1231.
19. Li, H., et al., *PEGylated ceria nanoparticles used for radioprotection on human liver cells under γ-ray irradiation.* Free Radical Biology and Medicine, 2015. **87**: p. 26-35.
20. Minarchick, V.C., et al., *Cerium dioxide nanoparticle exposure improves microvascular dysfunction and reduces oxidative stress in spontaneously hypertensive rats.* Frontiers in Physiology, 2015. **6**: p. 339.
21. Niu, J., et al., *Cardioprotective effects of cerium oxide nanoparticles in a transgenic murine model of cardiomyopathy.* Cardiovascular Research, 2007. **73**(3): p. 549-559.
22. Heckman, K.L., et al., *Custom cerium oxide nanoparticles protect against a free radical mediated autoimmune degenerative disease in the brain.* ACS Nano, 2013. **7**(12): p. 10582-10596.

23. Das, M., et al., *Auto-catalytic ceria nanoparticles offer neuroprotection to adult rat spinal cord neurons.* Biomaterials, 2007. **28**(10): p. 1918-1925.
24. Wong, L.L. and J.F. McGinnis, *Nanoceria as bona fide catalytic antioxidants in medicine: what we know and what we want to know…*, in *Retinal Degenerative Diseases*. 2014, Springer. p. 821-828.
25. Fiorani, L., et al., *Cerium oxide nanoparticles reduce microglial activation and neurodegenerative events in light damaged retina.* PLoS One, 2015. **10**(10): p. e0140387.
26. Chigurupati, S., et al., *Effects of cerium oxide nanoparticles on the growth of keratinocytes, fibroblasts and vascular endothelial cells in cutaneous wound healing.* Biomaterials, 2013. **34**(9): p. 2194-2201.
27. Hardas, S.S., et al., *Rat hippocampal responses up to 90 days after a single nanoceria dose extends a hierarchical oxidative stress model for nanoparticle toxicity.* Nanotoxicology, 2014. **8**: p. 155-166.
28. Yokel, R.A., et al., *Distribution, elimination, and biopersistence to 90 days of a systemically introduced 30 nm ceria-engineered nanomaterial in rats.* Toxicological Sciences, 2012. **127**(1): p. 256-268.
29. Yokel, R.A., et al., *Biodistribution and oxidative stress effects of a systemically-introduced commercial ceria engineered nanomaterial.* Nanotoxicology, 2009. **3**(3): p. 234-248.
30. Yokel, R.A., et al., *The yin: an adverse health perspective of nanoceria: uptake, distribution, accumulation, and mechanisms of its toxicity.* Environmental Science: Nano, 2014. **1**(5): p. 406-428.
31. Casals, E., et al., *Intrinsic and extrinsic properties affecting innate immune responses to nanoparticles: the case of cerium oxide.* Frontiers in Immunology, 2017. **8**: p. 970.
32. Grulke, E.A., et al., *Surface-controlled dissolution rates: a case study of nanoceria in carboxylic acid solutions.* Environmental Science: Nano, 2019. **6**(5): p. 1478-1492.
33. Yokel, R.A., et al., *Carboxylic acids accelerate acidic environment-mediated nanoceria dissolution.* Nanotoxicology, 2019. **13**(4): p. 455-475.
34. Yokel, R.A., et al., *Simulated biological fluid exposure changes nanoceria's surface properties but not its biological response.* European Journal of Pharmaceutics and Biopharmaceutics, 2019. **144**: p. 252-265.
35. Heckert, E.G., et al., *The role of cerium redox state in the SOD mimetic activity of nanoceria.* Biomaterials, 2008. **29**(18): p. 2705-2709.
36. Reed, K., et al., *Exploring the properties and applications of nanoceria: is there still plenty of room at the bottom?* Environmental Science: Nano, 2014. **1**(5): p. 390-405.
37. Singh, S., et al., *A phosphate-dependent shift in redox state of cerium oxide nanoparticles and its effects on catalytic properties.* Biomaterials, 2011. **32**(28): p. 6745-6753.
38. Deshpande, S., et al., *Size dependency variation in lattice parameter and valency states in nanocrystalline cerium oxide.* Applied Physics Letters, 2005. **87**(13): p. 133113.
39. Masui, T., et al., *Synthesis of cerium oxide nanoparticles by hydrothermal crystallization with citric acid.* Journal of Materials Science Letters, 2002. **21**(6): p. 489-491.
40. Zhang, Y., et al., *Formation and thermal decomposition of cerium-organic precursor for nanocrystalline cerium oxide powder synthesis.* Journal of Dispersion Science and Technology, 2007. **28**(7): p. 1053-1058.
41. Da Silva, M.P., et al., *CeO_2-catalyzed ozonation of phenol.* Journal of Thermal Analysis and Calorimetry, 2010. **102**(3): p. 907-913.
42. Wang, Z.L. and X. Feng, *Polyhedral shapes of CeO_2 nanoparticles.* The Journal of Physical Chemistry B, 2003. **107**(49): p. 13563-13566.

43. Mudunkotuwa, I.A. and V.H. Grassian, *The devil is in the details (or the surface): impact of surface structure and surface energetics on understanding the behavior of nanomaterials in the environment.* Journal of Environmental Monitoring, 2011. **13**(5): p. 1135-1144.
44. Li, Y., J.G. He, and X.W. Huang, *Synthesis and properties of cerium oxide nanoparticles.* Advanced Materials Research, 2011. **299**: p. 118-121.
45. Chandar, N.K. and R. Jayavel, *Synthesis and characterization of C_{14}TAB passivated cerium oxide nanoparticles prepared by co-precipitation route.* Physica E: Low-Dimensional Systems and Nanostructures, 2014. **58**: p. 48-51.
46. Darroudi, M., et al., *Green synthesis and evaluation of metabolic activity of starch mediated nanoceria.* Ceramics International, 2014. **40**(1): p. 2041-2045.
47. Tamizhdurai, P., et al., *Environmentally friendly synthesis of CeO_2 nanoparticles for the catalytic oxidation of benzyl alcohol to benzaldehyde and selective detection of nitrite.* Scientific Reports, 2017. **7**: p. 46372.
48. Xu, H., et al., *Synthesis of solid, spherical CeO_2 particles prepared by the spray hydrolysis reaction method.* Journal of the American Ceramic Society, 2002. **85**(1): p. 139-144.
49. Feng, X., et al., *Converting ceria polyhedral nanoparticles into single-crystal nanospheres.* Science, 2006. **312**(5779): p. 1504-1508.
50. Zhang, D., et al., *Synthesis of CeO_2 nanorods via ultrasonication assisted by polyethylene glycol.* Inorganic Chemistry, 2007. **46**(7): p. 2446-2451.
51. Jimmy, C.Y., L. Zhang, and J. Lin, *Direct sonochemical preparation of high-surface-area nanoporous ceria and ceria–zirconia solid solutions.* Journal of Colloid and Interface Science, 2003. **260**(1): p. 240-243.
52. Masui, T., et al., *Characterization of cerium(IV) oxide ultrafine particles prepared using reversed micelles.* Chemistry of Materials, 1997. **9**(10): p. 2197-2204.
53. Goharshadi, E.K., S. Samiee, and P. Nancarrow, *Fabrication of cerium oxide nanoparticles: characterization and optical properties.* Journal of Colloid and Interface Science, 2011. **356**(2): p. 473-480.
54. Kumar, E., P. Selvarajan, and D. Muthuraj, *Synthesis and characterization of CeO_2 nanocrystals by solvothermal route.* Materials Research, 2013. **16**(2): p. 269-276.
55. Baqer, A.A., et al., *Effect of polyvinylpyrrolidone on cerium oxide nanoparticle characteristics prepared by a facile heat treatment technique.* Results in Physics, 2017. **7**: p. 611-619.
56. Gu, H. and M.D. Soucek, *Preparation and characterization of monodisperse cerium oxide nanoparticles in hydrocarbon solvents.* Chemistry of Materials, 2007. **19**(5): p. 1103-1110.
57. Stark, W.J., *Nanoparticles in biological systems.* Angewandte Chemie International Edition, 2011. **50**(6): p. 1242-1258.
58. Dan, M., et al., *Ceria-engineered nanomaterial distribution in, and clearance from, blood: size matters.* Nanomedicine, 2012. **7**(1): p. 95-110.
59. Molina, R.M., et al., *Bioavailability, distribution and clearance of tracheally instilled, gavaged or injected cerium dioxide nanoparticles and ionic cerium.* Environmental Science: Nano, 2014. **1**(6): p. 561-573.
60. Bjondahl, K., *Differences in liver weight, mortality in cerium-treated mice and ^{144}Ce levels in blood, liver, urine and faeces at various intervals after treatment with nafenopin and pregnenolone 16-alpha-carbonitrile (PCN).* Medical Biology, 1976. **54**(6): p. 454-460.
61. Graca, J.G., F.C. Davison, and J.B. Feavel, *Comparative toxicity of stable rare earth compounds: acute toxicity of intravenous injections of chlorides and chelates in dogs.* Archives of Environmental Health: An International Journal, 1964. **8**(4): p. 555-564.
62. Nakamura, Y., et al., *Differences in behavior among the chlorides of seven rare earth elements administered intravenously to rats.* Toxicological Sciences, 1997. **37**(2): p. 106-116.

63. Yokel, R.A., et al., *Biodistribution and biopersistence of ceria engineered nanomaterials: size dependence.* Nanomedicine: Nanotechnology, Biology and Medicine, 2013. **9**(3): p. 398-407.
64. Cheng, Y., et al., *Formation of domain structure of erythrocyte membrane in Wistar rat fed with $CeCl_3$ per os.* Chinese Science Bulletin, 2000. **45**(5): p. 426-429.
65. Chen, C., P. Zhang, and Z. Chai, *Distribution of some rare earth elements and their binding species with proteins in human liver studied by instrumental neutron activation analysis combined with biochemical techniques.* Analytica Chimica Acta, 2001. **439**(1): p. 19-27.
66. Takada, K., *Effects of low doses of DTPA on the excretion and organ retention of ^{144}Ce in the rat.* Strahlentherapie, 1977. **153**(3): p. 195-199.
67. Takada, K. and M. Fujita, *Effects of DTPA on the excretion and tissue distribution of ^{144}Ce administered subcutaneously, intramuscularly and intravenously in rats.* Journal of Radiation Research, 1973. **14**(2): p. 187-197.
68. Bobtelsky, M. and B. Graus, *Cerous citrate complexes, their composition, structure and behavior.* Journal of the American Chemical Society, 1955. **77**(7): p. 1990-1993.
69. Leal, R., *Composition and stability constant of a complex of cerium and ammonium citrate at alkaline pH.* Journal of Inorganic and Nuclear Chemistry, 1959. **10**(1-2): p. 159-161.
70. Ohyoshi, A., et al., *A study of citrate complexes of several lanthanides.* Journal of Inorganic and Nuclear Chemistry, 1972. **34**(6): p. 1955-1960.
71. Baggio, R., et al., *Gadolinium and neodymium citrates: evidence for weak ferromagnetic exchange between gadolinium(III) cations.* Inorganic Chemistry, 2005. **44**(24): p. 8979-8987.
72. Müller, B., W. Kläger, and G. Kubitzki, *Metal chelates of citric acid as corrosion inhibitors for zinc pigment.* Corrosion Science, 1997. **39**(8): p. 1481-1485.
73. Vanhoyland, G., et al., *Characterization and structural study of lanthanum citrate trihydrate $[La(C_6H_5O_7)(H_2O)_2] \cdot H_2O$.* Journal of Solid State Chemistry, 2005. **178**(1): p. 166-171.
74. Zhou, R.-S., et al., *Syntheses, structures and magnetic properties of a series of 2D and 3D lanthanide complexes constructed by citric ligand.* Journal of Molecular Structure, 2008. **877**(1-3): p. 115-122.
75. Taguchi, M., et al., *Growth mechanism and surface chemical characteristics of dicarboxylic acid-modified CeO_2 nanocrystals produced in supercritical water: tailor-made water-soluble CeO_2 nanocrystals.* Crystal Growth & Design, 2009. **9**(12): p. 5297-5303.
76. Baggio, R. and M. Perec, *Isolation and characterization of a polymeric lanthanum citrate.* Inorganic Chemistry, 2004. **43**(22): p. 6965-6968.
77. Getsova, M., et al., *Cerium(III/IV) and Cerium(IV)–Titanium(IV) citric complexes prepared in ethylene glycol medium.* Monatshefte für Chemie/Chemical Monthly, 2007. **138**(5): p. 389-401.
78. Chen, M.-L., S. Gao, and Z.-H. Zhou, *Isolations and characterization of highly water-soluble dimeric lanthanide citrate and malate with ethylenediaminetetraacetate.* Dalton Transactions, 2012. **41**(4): p. 1202-1209.
79. Heller, A., et al., *Curium(III) citrate speciation in biological systems: a europium(III) assisted spectroscopic and quantum chemical study.* Dalton Transactions, 2012. **41**(45): p. 13969-13983.
80. Auffan, M., et al., *Long-term aging of a CeO_2 based nanocomposite used for wood protection.* Environmental Pollution, 2014. **188**: p. 1-7.
81. Hancock, M.L., *The fabrication and characterization of metal oxide nanoparticles employed in environmental toxicity and polymeric nanocomposite applications.* University of Kentucky Doctoral Dissertations, 2019.
82. Turner, S., et al., *High resolution mapping of surface reduction in ceria nanoparticles.* Nanoscale, 2011. **3**(8): p. 3385-3390.
83. Xiong, C. and S. Friedlander, *Morphological properties of atmospheric aerosol aggregates.* Proceedings of the National Academy of Sciences, 2001. **98**(21): p. 11851-11856.

84. López, J.M., et al., *The prevalence of surface oxygen vacancies over the mobility of bulk oxygen in nanostructured ceria for the total toluene oxidation.* Applied Catalysis B: Environmental, 2015. **174**: p. 403-412.
85. Veranitisagul, C., et al., *Novel recovery of nano-structured ceria (CeO_2) from Ce(III)-benzoxazine dimer complexes via thermal decomposition.* International Journal of Molecular Sciences, 2011. **12**(7): p. 4365-4377.
86. Sujana, M., K. Chattopadyay, and S. Anand, *Characterization and optical properties of nano-ceria synthesized by surfactant-mediated precipitation technique in mixed solvent system.* Applied Surface Science, 2008. **254**(22): p. 7405-7409.
87. Staggemeier, K.A., *The use of mesoporous silica as a template for the nanocasting of metal oxide arrays.* University of Alabama Doctoral Dissertations, 2015.
88. Wu, T.-S., et al., *X-ray absorption study of ceria nanorods promoting the disproportionation of hydrogen peroxide.* Chemical Communications, 2016. **52**(28): p. 5003-5006.
89. Larsen, E.K., et al., *Size-dependent accumulation of PEGylated silane-coated magnetic iron oxide nanoparticles in murine tumors.* ACS Nano, 2009. **3**(7): p. 1947-1951.
90. van Drunen, M., et al., *Measurement of cluster formation in aqueous citric acid solutions by photon correlation spectroscopy.* Journal of Crystal Growth, 1993. **134**(3-4): p. 196-202.
91. Wang, B., et al., *Influence of surface charge on lysozyme adsorption to ceria nanoparticles.* Applied Surface Science, 2012. **258**(14): p. 5332-5341.
92. McBride, J., et al., *Raman and X-ray studies of $Ce_{1-x}RE_xO_{2-y}$, where RE= La, Pr, Nd, Eu, Gd, and Tb.* Journal of Applied Physics, 1994. **76**(4): p. 2435-2441.
93. Riddick, T.M., *Control of Colloid Stability through Zeta Potential*. 1968: Livingston Wynnewood, PA.